Published in final edited form as:

J Neurosci. 2008 July 23; 28(30): 7637–7647. doi:10.1523/JNEUROSCI.1488-08.2008.

Mapping prefrontal circuits *in vivo* with manganese-enhanced MRI in monkeys

Janine M. Simmons[1], **Ziad S. Saad**[2], **Martin J. Lizak**[3], **Michael Ortiz**[1], **Alan P. Koretsky**[3], and **Barry J. Richmond**[1]

1 *Laboratory of Neuropsychology, National Institute of Mental Health, National Institutes of Health, Department of Health and Human Services, Bethesda, MD 20892*

2 *Scientific and Statistical Computing Core, National Institute of Mental Health, National Institutes of Health, Department of Health and Human Services, Bethesda, MD 20892*

3 *NMR Imaging Research Facility, National Institute of Neurological Disorder and Stroke, National Institutes of Health, Department of Health and Human Services, Bethesda, MD 20892*

Abstract

Manganese-enhanced magnetic resonance imaging (MEMRI) provides a powerful tool to study multi-synaptic circuits *in vivo*, and thereby to link information about neural structure and function within individual subjects. Making the best use of MEMRI in monkeys requires minimizing manganese-associated neurotoxicity, maintaining sensitivity to manganese-dependent signal changes, and mapping transport throughout the brain without *a priori* anatomical hypotheses. Here, we performed intracortical injections of isotonic $MnCl_2$, comparisons of pre- and post-injection scans, and voxel-wise statistical mapping. Isotonic $MnCl_2$ did not cause cell death at the injection site, damage to downstream targets of manganese transport, behavioral deficits, or changes in neuronal responsiveness. We detected and mapped manganese transport throughout cortical-subcortical circuits by using voxel-wise statistical comparisons of at least 10 pre- and 2 post-injection scans. We were able to differentiate between focal and diffuse projection fields and to distinguish between the topography of striatal projections from orbitofrontal and anterior cingulate cortex in a single animal. This MEMRI approach provides a basis for combining circuit-based anatomical analyses with simultaneous single unit recordings and/or fMRI in individual monkeys. Such studies will enhance our interpretations of functional data and our understanding of how neuronal activity is transformed as it propagates through a circuit.

Keywords

orbitofrontal cortex; anterior cingulate cortex; striatum; neuroanatomy; tract tracing; non-human primate

In vivo tract tracing makes it possible to study the topography, plasticity, and function of different neural circuits in individual subjects (Saleem et al., 2002; Silva et al., 2004). Manganese-enhanced magnetic resonance imaging (MEMRI) provides a promising tool for identifying neuronal circuits *in vivo* (Pautler et al., 1998; Pautler, 2004). Manganese enters neurons via calcium channels, is transported along microtubules, and crosses synapses. Manganese ions are paramagnetic and can be localized using T_1-weighted MRI (Silva et al.,

---

Corresponding Author: Barry J. Richmond, Building 49, Room 1B80, National Institute of Mental Health, Bethesda, MD 20892-4415, Phone: (301) 443-7319, Fax: (301) 402-0046, E-mail: bjr@ln.nimh.nih.gov.

2004). Multi-synaptic neuronal circuits have been visualized after intracerebral injections of manganese chloride ($MnCl_2$) in birds, rats and monkeys (Sloot and Gramsbergen, 1994; Saleem et al., 2002; Van der Linden et al., 2002; Pautler et al., 2003; Watanabe et al., 2004; Murayama et al., 2006).

To make the best use of MEMRI, three technical issues must be addressed: manganese toxicity, manganese detection, and mapping of manganese transport. First, manganese is neurotoxic. Manganese overexposure leads to a parkinsonian-like syndrome in humans (Pal et al., 1999). In monkeys, systemic manganese injections lead to parkinsonian symptoms, basal ganglia pathology, and reductions in dopaminergic enzymes and receptors (Eriksson et al., 1987; Eriksson et al., 1992; Olanow et al., 1996). Striatal injections of $MnCl_2$ lead to reduced ATP and neurotransmitter levels in rats (Brouillet et al., 1993). Manganese neurotoxicity might interfere with the interpretation of neuroanatomical data (Canals et al., 2008) and might damage regions in which electrophysiological recordings are planned.

One way to decrease manganese neurotoxicity is to decrease the concentration of $MnCl_2$ injected (Canals et al., 2008). However, decreasing the $MnCl_2$ concentration makes detecting manganese-dependent changes in T_1-weighting more difficult (Silva et al., 2004). Compensating for a lower $MnCl_2$ concentration presents several technical challenges. For example, high-Tesla magnets may not have bore diameters large enough to accommodate monkeys. Longer and/or repeated scans could increase the time of each experiment and the physiological burden on each subject.

To be most useful, MEMRI should make it possible to map the known axonal projections in a particular individual and to detect previously unidentified circuits. However, previous MEMRI studies have relied on region-of-interest analyses, group analysis, and/or normalizations of signal intensities to control brain regions (Watanabe et al., 2001; Saleem et al., 2002; Van der Linden et al., 2002; Leergaard et al., 2003; Pautler et al., 2003; Van Meir et al., 2004; Bilgen et al., 2006; Murayama et al., 2006; van der Zijden et al., 2007; Canals et al., 2008). Region-of-interest analyses can be limited by *a priori* anatomical hypotheses. Group averages may obscure individual neuroanatomical differences in monkeys. Because Mn^{2+} is transported transynaptically, it may be difficult to choose reliably manganese-free control regions for signal normalization.

In this study, we have addressed each of these three challenges. We have identified and used a non-toxic concentration of $MnCl_2$. We have improved our ability to detect manganese transport by comparing post- to pre-injection scans. We have adapted an analytical technique from fMRI to provide unbiased maps of manganese transport from two regions of prefrontal cortex.

MATERIALS AND METHODS

Animals

Three monkeys were used in these experiments: 1 male rhesus (P: 5–5.5 kg), 1 male cynomolgus (S: 5 kg), 1 female cynomolgus (T: 4.6–6 kg).

Surgery

We implanted magnet-compatible recording chambers and head fixation posts (Cilux recording chambers and PEEK head holders from Crist Instrument Co., Inc., Hagerstown, MD; ceramic screws from Thomas Recording GmbH, Giessen, Germany) using sterile surgical procedures. Surgeries took place under general anesthesia in a veterinary operating facility. Craniotomy and chamber locations were determined from pre-surgical magnetic resonance images (MRIs) of each animal's brain. All procedures were carried out according to NIH guidelines and approved by the National Institute of Mental Health Animal Care and Use Committee.

Manganese chloride injections

We made micro-injections of manganese chloride ($MnCl_2 \cdot 4H_2O$;Sigma-Aldrich Co., MO) into orbitofrontal and anterior cingulate cortex. Injections were made with a 0.5μL Hamilton syringe (Hamilton Co., Reno, NV), through recording grids with 1mm spacing (Crist Instruments Inc., Hagerstown, MD). Concentrations of $MnCl_2$ were either 800 mM or 120 mM in sterile water. Total volumes of $MnCl_2$ ranged between 0.2 and 0.5 μL (Table 1). $MnCl_2$ solutions were not buffered. Injections were made extremely slowly, over 20–30 minutes (e.g., at a rate of 0.01 to 0.25 μL/minute). During injections, monkeys were sedated with ketamine (10 mg/kg IM) and medetomidine (20 μg/kg IM).

MRI Data Acquisition

We obtained MR images regularly throughout this study to determine initial recording chamber placement and to localize injection and recording sites. Because we required stereotaxic coordinates for these scans and the bore size of the 4.7T magnet did not accommodate our magnet-compatible stereotaxic head holder, these MRIs were obtained on a 1.5T GE Signa unit. We used a 5-inch GP surface coil and a 3D volume SPGR pulse sequence (TE 6, TR 25, flip angle 30, FOV of 11 cm, slice thickness of 1mm).

We obtained high-resolution images for MEMRI analyses on a horizontal Bruker 4.7T MRI system (Bruker Biospin MRI GmBH, Ettlingen, Germany) using a custom-made oval surface coil (10 cm × 12 cm) for transmit and receive. All images were acquired with a gradient echo pulse sequence and nominal isotropic resolution of 0.5 mm^3. One or more MRIs for each animal were obtained to highlight gray-white matter contrast and identify anatomical landmarks (TR 100 msec, TE 6.5 msec, apparent flip angle 10°). To optimize contrast due to $MnCl_2$, sequence parameters were: TR 100 msec, TE 3.5–4.7, apparent flip angle 45°.

We obtained a series of pre-injection baseline MRIs with the $MnCl_2$ sequence parameters prior to the 120mM $MnCl_2$ injections. Post-injection scans were obtained immediately after the injection (Day 0), on Day 2 and/or 4, and/or 7 (Table 1). Across scanning sessions, precise measurements and markers were used to ensure consistent placement of the monkey's head in the head holder, the surface coil relative to the monkey's head, and the monkey's head within the magnet. Each scan was aligned to the AC-PC line to facilitate subsequent automated volume registration.

During all MR sessions, monkeys were sedated with ketamine (initial dose 10 mg/kg IM; subsequent doses 5 mg/kg IM every 30–40 minutes) and medetomidine (20 μg/kg IM every 60–80 minutes). Heart rate, temperature and blood oxygenation were monitored, and heart rate maintained with glycopyrrolate (15μg/kg IM prior to first dose of ketamine and every 3 hours thereafter as needed).

MRI Data Analyses

Signal enhancements due to Mn^{2+} uptake and transport were easily seen by eye after injections of high concentration $MnCl_2$ (800 mM). Because of the strong contrast in these volumes, we simply applied a reasonable non-quantitative threshold and used a color lookup table available in ImageJ (Abramoff et al., 2004) to highlight the areas of Mn^{2+} transport.

We could not detect Mn^{2+} transport after injections of isotonic $MnCl_2$ (120 mM)without additional analyses to increase sensitivity. To do so, we compared signal intensities in post- versus pre-injection volumes. Such comparisons could have been made simply by taking the difference at every voxel between one post-injection and one pre-injection scan. However, such a simple approach would fail to take into account the signal variance arising at each voxel due to differences between individual scans and across scanning sessions. The noise present in MR imaging introduces signal changes during each scan that are unrelated to Mn^{2+} transport. Moreover, because the Mn^{2+}-related signal is weaker with lower concentrations of $MnCl_2$, noise-induced signal changes may become comparable in size to Mn^{2+}-related signal enhancements.

Therefore, we used an approach designed to obtain estimates of the variance in both pre- and post-injection scans. We first collected a set of pre-injection scans (N_{pre}) over a period of days before the $MnCl_2$ injections. On the day of injection, we acquired one scan, merely to verify the site of injection. For each subsequent post-injection day, we obtained two successive scans (N_{post}) to allow for statistical testing of signal enhancements due to Mn^{2+}. All pre- and post-injection images were obtained using the same scanning setup and parameters.

Table 1 shows the number and chronology of pre- and post-injection scans for each of the subjects in this study. Note that while it is obviously best to obtain a large number of pre-injection scans and repeated acquisitions of post-injection scans at each time point, the availability of dedicated time on the magnet, the duration and complexity of the scanning procedure itself, and our concerns for the welfare of the monkeys placed practical limitations on the experimental design. The acquisition of each high-resolution image took 1 hour 47 minutes. Taking into consideration animal preparation time, tuning and shimming requirements, and anesthesia limitations, we were able to acquire two full high-resolution volumes during a 4–5 hour scanning session. We scheduled scanning sessions twice weekly for approximately three weeks prior to the $MnCl_2$ injections. Therefore, for each animal, we obtained 10–12 pre-injection scans and 2 scans at each post-injection time point.

AFNI was used for image processing and analyses (Cox, 1996; Cox and Hyde, 1997). Preprocessing steps were carried out as follows. First, the skull was stripped from each pre- and post-injection scan using AFNI's 3dSkullStrip program. All skull-stripped pre-injection scans were then registered together using non-rigid 12-parameter affine transforms and an average pre-injection volume was calculated. This average pre-injection volume was then used as a reference for registering anew all the original pre-injection scans. Post-injection volumes were also registered to the average pre-injection volume at this stage. Once registered, image non-uniformity was reduced using AFNI's 3dUniformize and a spatial smoothing of 1mm full-width at half-maximum (FWHM) was applied to increase the signal-to-noise ratio. Each volume was then normalized to its own mean voxel intensity to correct for scanner amplifier gain differences between scans. At this stage, we had a set of pre-injection scans in register, with image non-homogeneity reduced, and scaled to the same mean intensity. The next step consisted of ascertaining where there was significant signal enhancement in the post-injection scans on a voxel-wise basis.

For each post-injection time point, we used a two-sample t-test to compare the signal intensity in the two post-injection scans to that in the pre-injection scans on a voxel-wise basis. Given the small sample size and the potential for artifacts, we also confirmed our results with a non-parameteric permutation technique. We took the total number of pre- and post-injection scans ($N_{total} = N_{pre} + N_{post}$) and compared the mean of any two of those scans ($k=2$) to the mean of the remaining scans. At each voxel, we calculated the difference between the means for each of the possible C combinations of scans ($C = N$ choose 2 combinations $= N!/k!(N-k)!$). We then mapped those voxels for which the biggest difference occurred when the scan sets contained the true pre- and post-injection scans. The difference between the means at each of those voxels served as a measure of the degree of signal enhancement. The probability of finding signal enhancement by chance alone in any particular voxel with this technique depends upon the total number of scans and the number of possible combinations. Specifically, p = 1/ C voxel-wise (for monkey S, p = .015; for monkey T, p =.011). We found that images obtained using this non-parametric method corroborated our findings using the t-test at the same p value. Because the parametric statistics allowed us greater flexibility to localize and compare Mn^{2+} signal enhancements at different thresholds, we used the t-test results in generating all further Mn^{2+} transport maps.

After obtaining the voxel-wise statistics, we corrected for false positives due to multiple comparisons by enforcing spatial constraints on the signal enhancement maps. This family-wise correction method uses spatial smoothness estimates of the noise in the data to determine the likelihood of observing spatial clusters of various sizes. The spatial smoothness of the noise was estimated from pre-injection images, after removing anatomical spatial structure by voxel-wise low order trending of the series of pre-injection scans. The FWHM of the smoothing filter was then estimated per the method described by Forman et al., 1995 using AFNI's 3dFWHMx program (Forman et al., 1995). With this measure of spatial smoothness, the number of brain voxels in each image, and a given voxel-wise probability of false-positives, we could use a AFNI's AlphaSim program to perform a Monte-Carlo simulation and estimate the probability of obtaining clusters of a particular size by chance alone. We then corrected for multiple comparisons by rejecting spatial clusters smaller than what would be expected by chance. For both monkeys, the minimum cluster size threshold was set such that the corrected p-value of the signal intensity maps was $p <= .01$ (monkey S: 375 voxels; monkey T: 285 voxels).

This method allows us to measure MEMRI signal intensities across an entire brain volume after a single injection of $MnCl_2$ in an individual animal. After any particular injection, signal intensities can be displayed as projection density maps and compared across transport sites or time. As with any tract tracing technique, variability in uptake and transport inevitably arises from differences in injection placement, from small changes in neuronal density at the injection site, and/or from largely unpredictable metabolic changes that affect tracer absorption and diffusion. Thus, the patterns in the projection density maps can be compared across animals or injections, but the absolute signal intensity values themselves cannot be compared.

Behavioral and Electrophysiological Testing

Behavioral testing and electrophysiological recording began after completion of the $MnCl_2$ injections and post-injection MRI sessions. In S, the two weeks of daily sessions began ten days after the last orbitofrontal injection. In T, behavioral and recording sessions began 23 days after the orbitofrontal injection and lasted three weeks.

In all behavioral sessions, monkeys responded to visual stimuli presented on a computer display monitor. Behavioral control and data acquisition were performed using the REX program (Hays et al., 1982). Neurobehavioral Systems Presentation software was used to display visual stimuli (Neurobehavioral Systems, Inc., Albany, CA). Licking data were obtained through a strain gauge attached to the sipper tube through which liquid was delivered.

The monkeys were exposed to a classical conditioning paradigm in which visual stimuli were presented on a computer monitor in random order. One visual cue (CS+) was followed by a liquid reward; after the other visual stimulus (CS−), there was no reward (Fig. 1A). We measured the proportion of CS+ versus CS− trials with anticipatory licking.

Single unit recordings were obtained from orbitofrontal cortex while the monkeys performed this task. All well-isolated single unit action potentials were recorded and included in the data analyses. Action potentials were converted to pulses using a time-voltage window discriminator (FHC Inc., Bowdoin, ME) and were recorded at 1 millisecond resolution with Rex.

Histology

At the completion of these experiments, all monkeys were transcardially perfused with 4% paraformaldehyde and the brains removed for histological processing. P's brain was obtained one year after the first $MnCl_2$ injection and one month after the last injection. S's brain was obtained six months after the first $MnCl_2$ injection and 23 days after the last injection. T's brain was obtained four months after the $MnCl_2$ injection.

Brains were cryoprotected in a solution of 10% glycerol and 2% DMSO in 0.1M phosphate buffer for 24 hours and then a transferred to a 20% glycerol solution for five days. Brains were blocked and frozen using isopentane at −80°C. Coronal sections were cut at 40 μm on a freezing microtome. Sections were taken from the frontal pole through to the rostral cerebellum. Separate series of sections were processed for Nissl substance, cytochrome oxidase, and/or tyrosine hydroxylase. Within each series, adjacent sections were within 400 μm.

The cytochrome oxidase incubation solution consisted of 0.5 mg/mL Cytochrome C, 100 mg/mL sucrose, 0.25 mg/mL DAB (3,3′-dioaminobenzidine tetrahydrochloride tablets), and 0.1 mg/mL catalase in 0.1M phosphate-buffered saline at pH 7.4. All cytochrome oxidase reagents were obtained from Sigma-Aldrich, St. Louis, MO.

For tyrosine hydroxylase (TH) immunohistochemistry, we incubated the sections with primary antibody (mouse anti-TH from Chemicon, Temecula, CA) overnight at room temperature, with secondary antibody (anti-mouse IgG made in horse, ABC Elite Kit, Vector Laboratories, Burlingame, CA) and BSA (Bovine Serum Albumin, Sigma-Aldrich, St. Louis, MO) for one hour, and with solutions from the Vectastain ABC Elite Kit (Vector Laboratories, Burlingame, CA) for 90 minutes. Sections were developed with DAB (3,3′-dioaminobenzidine tetrahydrochloride tablets, Sigma-Aldrich, St. Louis, MO).

RESULTS

High concentration $MnCl_2$ (800 mM)

Manganese transport—Injections of 800 mM $MnCl_2$ were made into orbitofrontal cortex (OFC) on three separate occasions over a one-year period in one animal (P; Table 1). Changes in signal intensity due to manganese (Mn^{2+}) were visible to the naked eye on the MRIs obtained within three hours of these injections (Day 0). Injections were centered in and covered most of OFC area 13 (Fig. 2A). Increases in signal intensity due to Mn^{2+} transport were also visible by eye on post-injection Day 4 (Fig. 2B–D). Mn^{2+} signal was detected throughout the cortical-striatal-thalamic loop, to areas including ventrolateral caudate and ventromedial putamen, globus pallidus externa and interna, ventral pallidum, substantia nigra, mediodorsal nucleus of the thalamus and habenula. Mn^{2+} enhancement was also visible in white matter tracts, most notably in the internal capsule between OFC and the ventral striatal region. These imaging results confirm that specific cortical-subcortical projections can be mapped using intracortical injections of high concentration $MnCl_2$ in monkeys (Saleem et al., 2002).

Histology—Thionin staining revealed areas of complete cell loss after high concentration $MnCl_2$ injections. Two separate lesion sites were observed, corresponding in location to the second and third injection sites (Fig. 3A). Because the first and second injection sites overlapped significantly, tissue damage resulting from these two injections was most likely coextensive.

The size of each lesion was smaller than the spread of Mn^{2+} seen at the corresponding injection site on Day 0. For example, the MEMRI taken on Day 0 showed an injection site measuring approximately 7.5 mm × 3 mm × 5 mm (Fig. 2A) while the corresponding area of cell loss measured 2.3 mm × 1.2 mm × 1.6 mm (Fig. 3B). This result suggests that cell death occurred only within the areas of peak Mn^{2+} concentration near the tip of the Hamilton syringe. Downstream targets of Mn^{2+} transport appeared histologically intact, with no observable loss of tyrosine hydroxylase activity in striatum (Fig. 3C). These histological results demonstrate that intracortical injections of high concentration $MnCl_2$ at sub-microliter volumes can cause local neuronal toxicity and cell death.

Isotonic $MnCl_2$ (120 mM)

Manganese transport—Injections of 120 mM $MnCl_2$ were made in two monkeys (S & T; Table 1). S received three separate injections over four months, two in OFC and one in anterior cingulate cortex (ACC). T received a single injection in OFC. In order to detect the low levels of Mn^{2+} transported, voxel-wise statistical comparisons of post- to pre-injection signal intensities were performed. Scans of adequate quality for this analysis were obtained on Days 0, 2, and 4 after the OFC injections and on Days 0, 4, and 7 after the ACC injection (Table 1). In all cases, Mn^{2+} transport was observed within cortical-striatal-thalamic loops.

Orbitofrontal Injections

$MnCl_2$ injections into OFC were localized to the lateral half of area 13 in both T and S (Fig. 4A, B). On post-injection Day 2 (Fig. 5), enhancements due to Mn^{2+} were found ipsilaterally in more widespread regions of OFC, including most of areas 11 and 13. Subcortical transport of Mn^{2+} to striatum was detected in the head of the caudate nucleus, in most of the rostral putamen, ventrolaterally in the body of the caudate (in monkey S) and/or ventromedially in the more caudal putamen (in both). Mn^{2+} transport to globus pallidus externa was also detectable by Day 2 (greater in monkey S than monkey T). In both animals, enhancements due to Mn^{2+} were seen in the mediodorsal nucleus of the thalamus by Day 2 (again, greater in monkey S than T). In monkey S only, Mn^{2+} signal also appeared in the ventral anterior nucleus of the thalamus.

On post-injection Day 4 (Fig. 6 and selected larger views in online supplemental material), Mn^{2+} signal persisted in OFC areas 11 and 13. In monkey S, cortico-cortical Mn^{2+} transport was also observed in ipsilateral dorsolateral prefrontal cortex (dlPFC, area 46), ipsilateral anterior cingulate cortex (areas 24 and 32; not shown), and bilateral insular cortex (IC). Subcortical signal persisted in the rostral putamen, as well as in regions of ventrolateral caudate and/or ventromedial putamen in both animals. Transport to globus pallidus externa and ventral pallidum was also detected in both animals on Day 4, with greater signal intensity in monkey S. Mn^{2+} signal in thalamus was no longer detectable on Day 4 in either monkey. Overall, these results are very similar to those obtained with high concentration $MnCl_{2,}$ demonstrating that isotonic $MnCl_2$ can be used successfully for *in vivo* tract tracing in monkeys.

We compared the intensity and extent of Mn^{2+} signal between post-injection Days 2 and 4, and found four trends (Figs. 5, 6, and 7). First, transport of Mn^{2+} from OFC to direct and trans-synaptic subcortical targets could be detected by post-injection Day 2 (Fig. 5). Secondly, there was extensive regional overlap of the Mn^{2+} signal on Days 2 and 4; we found no additional subcortical regions with enhanced signal intensity due to Mn^{2+} on Day 4 (Fig. 7). Thirdly, the signal intensity at the injection site and in subcortical targets decreased from Day 2 to Day 4 (compare Figs. 5 and 6). In contrast, we observed a wider spread of Mn^{2+} signal in cortical target regions on Day 4 than Day 2 in monkey S.

Anterior Cingulate Injection

The $MnCl_2$ injection into ACC was located just ventral to the cingulate sulcus in area 24c (Fig. 4C). On Day 4 (Fig. 8 left and selected larger views in online supplemental material), Mn^{2+} transport was detected through most of ipsilateral areas 24c, as well as being seen in other sub-regions on the medial wall (areas 24b and 32). Cortico-cortical projections to ipsilateral dorsolateral prefrontal and orbitofrontal cortex were also observed. Ipsilateral subcortical transport sites included dorsal caudate and putamen. Mn^{2+} enhancement was also visible in white matter tracts, most notably in the corpus callosum at the level of the rostral striatum and in the internal capsules bilaterally. The Mn^{2+} signal extended from the ACC across the corpus callosum to the contralateral putamen. Mn^{2+} signal was observed bilaterally in globus pallidus externa and ventral pallidum, with stronger signal ipsilaterally. Mn^{2+} transport was also detected in the ipsilateral globus pallidus interna. Finally, Mn^{2+} signal appeared in the thalamus, in the medial dorsal and ventral anterior nuclei.

On post-injection Day 7 (Fig. 8 right), Mn^{2+} signal had decreased in intensity and spatial extent at the injection site and in subcortical target regions. Signal did persist ipsilaterally in dorsal caudate and putamen and in globus pallidus externa and interna.

These results demonstrate that, as expected, MEMRI can be used to map cortical-subcortical circuits from more than one cortical region in a single animal. A comparison of the anterior cingulate data to those obtained after the orbitofrontal injections reveal differences in the topographic distributions of the cortical-striatal projections on post-injection Day 4 (Figs. 6, 8, and 9). In general, the Mn^{2+} signal is detected more rostrally, ventrally, and medially after injections in OFC than after ACC injections. Specifically, area 13 of OFC projects most strongly to the ipsilateral ventrolateral striatum and ventromedial putamen via the internal capsule. Area 24c of ACC projects most strongly to dorsal striatum and putamen. In addition, ACC sends projections through the corpus callosum to the contralateral striatum. Transynaptic projections to globus pallidus and thalamus from OFC and ACC are less differentiable.

Behavior—None of the three monkeys showed any obvious motor or social deficits. They moved well, took and ate treats, and showed normal social reactions to other monkeys and to the experimenters. S and T also performed normally in a classical conditioning paradigm with significantly more anticipatory licking in CS+ than CS− trials (Fig. 2B,C; S: 85.4% CS+ trials vs. 21.9% CS− trials, χ^2=1450.8, df = 1, p<.001; T: 37.2% CS+ trials vs. 25.1% CS- trials, χ^2=50.46, df =1, p<.001). Therefore, as expected, small $MnCl_2$ injections in OFC and ACC did not interfere with monkeys' ability to discriminate visual stimuli or to form correct stimulus-reinforcer associations.

Electrophysiological Recordings—A total of 100 OFC single neurons were recorded (40 in S; 60 in T) while the two monkeys performed in the classical conditioning paradigm. Neurons were isolated in a series of recording tracks surrounding the $MnCl_2$ injection site in each monkey. In both monkeys, tracks were located 1–2 mm from the injection site. In T, attempts were also made to obtain recordings at the injection site itself: only one OFC neuron was isolated in this track. The most likely explanation for the inability to isolate neurons in this recording track is that the Hamilton syringe needle itself caused local tissue damage and gliosis. In S, no neurons were found in one recording track located 1.4 mm from the injection site in the medial and caudal direction. It is possible that this track fell within an area of physical damage visible histologically (see Fig. 11).

In all other recording tracks, healthy neurons were easily isolated and held. The neuronal density (T: 4.9 +/− 0.1 neurons/mm in 9 tracks; S: 4.7 +/− 0.4 neurons/mm in 6 tracks) was consistent with that obtained previously from OFC in two monkeys without $MnCl_2$ injections (M1: 4.6 neurons/mm; M2: 6.3 neurons/mm; unpublished data). OFC neurons surrounding the $MnCl_2$ injection site were also responsive to events in the classical conditioning paradigm (Fig. 10). 73/100 neurons showed a significant change in firing rate after one or more of the task events (pre- vs post-event firing rates; 2-tailed, paired t-tests, p < .05); 45/100 showed significant differences in firing rate between the CS+ and CS− trials (2-way ANOVA; main effect of condition; p < .05). These results demonstrate that OFC neurons located near isotonic

$MnCl_2$ injection sites retain one of their primary response characteristics—selectivity to outcome contingencies (Thorpe et al., 1983;Tremblay & Schultz, 2000;Simmons & Richmond, 2008)

Histology—Thionin staining revealed no evidence of structural cell loss at any of the orbitofrontal injection sites in S or T (Fig. 11A, B). At the ACC injection site in S, thionin staining showed a small area of cell loss (Fig. 11C). Cellular metabolism at the OFC injection site in T appeared unimpaired on cytochrome oxidase labeled sections (Fig. 11A). In S, cytochrome oxidase levels appeared decreased in small regions near the injection sites (Fig. 11B, C). In all cases, injections of isotonic $MnCl_2$ caused much less damage at the injection sites than that seen with high concentration injections. Because downstream targets of Mn^{2+} transport remained histologically intact after injections of high concentration $MnCl_2$, we have assumed that the transport of lower concentrations of $MnCl_2$ would be equally non-toxic, if not less toxic.

DISCUSSION

This study confirms that MEMRI can be used to map multi-synaptic neuronal circuits *in vivo* in non-human primates (Saleem et al., 2002; Murayama et al., 2006). Intracortical injections of high-concentration $MnCl_2$ result in excellent transport with high signal intensities throughout the entire cortical-subcortical-thalamic loop. Therefore, as a first-pass technique to look for circuit connections *in vivo*, tract tracing with high-concentration $MnCl_2$ could be useful.

We investigated the histological effects of high-concentration $MnCl_2$ injections and found local cell death and discrete lesions at the injection sites. These findings are consistent with the known neurotoxicity of $MnCl_2$ (Eriksson et al., 1987; Eriksson et al., 1992; Olanow et al., 1996) and highlight the limitations of experiments using high-concentration MEMRI. Specifically, the lesions caused by high-concentration $MnCl_2$ are incompatible with the use of MEMRI for longitudinal studies and within-subject experimental designs.

We have developed an MEMRI protocol using intracortical injections of isotonic $MnCl_2$. This protocol avoids manganese-associated neurotoxicity, retains sensitivity to the T_1-weighted signal changes, and allows unbiased mapping of manganese transport. We found that isotonic $MnCl_2$ did not appear to cause cell death at the injection sites. Decreases in cellular metabolism at the injection sites, as assessed by cytochrome oxidase staining, were either small or not detectable. Single unit recordings demonstrated that OFC neurons around the injection sites were appropriately responsive to differences in outcome contingencies.

Utilizing isotonic $MnCl_2$ minimizes neurotoxicity, but also reduces the detectability of manganese transport. We solved this problem by building on a standard technique from the functional imaging field: we performed a set of voxel-wise comparisons between post- and pre-injection scans. We found that the use of pre-injection scans and statistical comparisons significantly improved our ability to detect manganese signal after injections of isotonic $MnCl_2$. We acquired MR data in a 4.7T magnet and included at least ten pre-injection scans and two post-injection scans from each time point in our analyses. In lower magnetic fields, such as the 3T magnets more commonly available, more pre-injection images might be needed to obtain adequate signal-to-noise. Acquiring the needed number of pre-injection scans is well worth the time and effort expended. Having these scans made it possible here to visualize manganese transport at half-millimeter resolution with individual scan times of less than two hours. The resulting transport maps of the orbitofrontal-subcortical circuit corresponded nicely to those obtained with high concentration $MnCl_2$.

The whole-brain statistical thresholding method used in this study not only allowed us to visualize cortical-subcortical circuits in individual animals with isotonic $MnCl_2$ injections, but also provided a measure of the relative density of projections within each region. Therefore, within a structure, we can differentiate between focal and diffuse projection fields (see Haber et al., 2006). For example, although the projection fields from orbitofrontal cortex to striatum overlapped with those from anterior cingulate cortex in this study, the projection from orbitofrontal cortex was most intense ventrally, whereas the projection from anterior cingulate cortex was most intense dorsally (see Kunishio & Haber, 1994; Ferry et al., 2000). The creation and comparison of such projection density maps would not be possible using a region-of-interest approach without precise *a priori* information.

The time course with which Mn^{2+} signal could be detected in sub-cortical regions after cortical injections of isotonic $MnCl_2$ was largely consistent with that seen with high concentration $MnCl_2$ injections (Saleem et al., 2002). That is, we could detect Mn^{2+} transport to direct striatal target regions and to transynaptic regions such as globus pallidus between post-injection Days 2 and 7. In our hands, however, the peak sub-cortical signal intensities were observed on Day 2 rather than Day 4, and signal intensities decreased with time in these regions. The seemingly surprising result that Mn^{2+} transport could be detected earlier with lower concentration injections may be due to toxicity-related cell death and transport blockade caused by high concentration $MnCl_2$ (Canals et al., 2008). It could also be due to the improved sensitivity of our imaging analyses. The decreases in signal intensity with time may result from limitations to signal detection at lower concentrations of $MnCl_2$.

Obtaining multiple scans and comparing T_1-weighted signal intensities between post- and pre-injection scans was key to detecting low concentrations of Mn^{2+} at remote sites in the present work with monkeys. Recently, it has been demonstrated that very low concentrations of Mn^{2+} could be detected along the olfactory pathway of individual rats using a fast, quantitative T_1 mapping technique that does not require repeated scans or statistical comparisons (Chuang & Koretsky, 2006). This work had the advantages of being performed at a higher field and on the smaller rodent brain. Currently, the time needed to acquire a full brain volume may be too long to allow such an approach with monkeys, but this alternative bodes well for the future.

As with any new methodology, additional technical improvements can and will be made. Advances in image acquisition techniques, such as the use of parallel MRI with multi-coil arrays already offer the likelihood that higher resolution images can be obtained more quickly (DeZwart et al., 2004). Faster scan times would allow the acquisition of more data per scanning session. With the analytical methods used in the present study, signal detection could be improved by using parallel MRI to acquire more pre- and post-injection scans for comparison. Alternatively, parallel MRI could be used to obtain fast quantitative T_1 maps of the entire monkey brain in a reasonable amount of time.

Faster scan times should make it feasible to obtain temporally more precise measurements of post-injection manganese transport and to answer critical questions regarding direct versus trans-synaptic transport and the precise connectivity of different circuits. In the present study, for example, we have seen early transport to thalamic nuclei that may reflect direct cortico-thalamic rather than cortico-striato-thalamic projections. Conversely, manganese signal in cortical regions distal to the injection site appeared later in time. It may take longer for manganese to reach detectable levels in cortex because cortical afferents are more diffusely distributed or because the path is trans-synaptic, perhaps even via subcortical structures.

The ability to study neuronal circuits *in vivo* provides a huge advantage in non-human primate research, in which each subject is particularly valuable. Neuroanatomical studies with conventional tract tracers can require 10–20 monkeys to map several different circuits or to follow a single transynaptic pathway (see Selemon and Goldman-Rakic, 1985; Eblen and Graybiel, 1995; Haber et al., 1995; Ferry et al., 2000; Haber et al., 2006). Using viral tract tracers that are transported transneuronally can reduce the number of monkeys needed to visualize a multisynaptic circuit, but this technique still requires sacrifice of the monkeys (Strick and Card, 1992; Hoover and Strick, 1993; Kelly and Strick, 2000). With MEMRI, we can outline an entire cortical-subcortical circuit at a single point in time, in an individual living monkey.

Our results show that MEMRI can be used to map and compare the distributions of multiple neuronal circuits sequentially in a single animal. Although the spatial resolution provided by MEMRI is regional rather than cellular, we have shown that this technique can distinguish between striatal projections from orbitofrontal cortex and anterior cingulate cortex. Because manganese is visible in axonal fibers as well as at synaptic terminals, the precise anatomical interpretation of MEMRI signal in a particular area may require independent confirmation with a technique that can differentiate synaptic terminals from fibers of passage. The projection patterns and putative synaptic sites we have seen after $MnCl_2$ injections in orbitofrontal and anterior cingulate cortex are consistent with those obtained with conventional tract tracers (Kunishio and Haber, 1994; Ferry et al., 2000).

MEMRI opens up the possibility of using neuroanatomical maps obtained from an individual animal under study to guide or interpret physiological experiments. For example, combining MEMRI with BOLD-signal based functional MRI should make it possible to super-impose maps of anatomical connectivity on maps of correlated activity patterns from the same animal.

MEMRI can also be combined with single-unit electrophysiological recordings. In this experiment, we injected isotonic $MnCl_2$ into orbitofrontal cortex and later recorded from neurons around the injection site. Similarly, MEMRI could be used to guide electrode placements in projection target zones, such as the basal ganglia nuclei receiving projections from OFC. Moreover, our quantitative analysis allows us to identify and target the sub-regions receiving the densest projection from any particular injection site in any given animal. The signal correlations obtained from simultaneous recordings in two or more densely connected regions will provide valuable constraints for theoretical and computational models that seek to explain how neuronal activity is transformed as it propagates forward through a circuit.

Supplementary Material

Refer to Web version on PubMed Central for supplementary material.

Acknowledgements

Funding provided by the Intramural Research Programs of NIMH and NINDS, and a NARSAD Young Investigator Award (JMS). Gang Chen, Bob Cox, David Ide, Megan Malloy, Hellmut Merkle, David Yu, Charles Zhu.

References

Abramoff MD, Magelhaes PJ, Ram SJ. Image Processing with ImageJ. Biophotonics International 2004;11:36–42.

Bilgen M. Imaging corticospinal tract connectivity in injured rat spinal cord using manganese-enhanced MRI. BMC Med Imaging 2006;6:15. [PubMed: 17112375]

Brouillet EP, Shinobu L, McGarvey U, Hochberg F, Beal MF. Manganese injection into the rat striatum produces excitotoxic lesions by impairing energy metabolism. Exp Neurol 1993;120:89–94. [PubMed: 8477830]

Canals S, Beyerlein M, Keller AL, Murayama Y, Logothetis NK. Magnetic resonance imaging of cortical connectivity *in vivo*. NeuroImage. 200810.1016/j.neuroimage.2007.12.007

Chuang K-H, Koretsky A. Improved neuronal taract tracing using manganese enhanced magnetic resonance imaging with fast T_1 mapping. Magn Reson Med 2006;55:604–11. [PubMed: 16470592]

Cox RW. AFNI: software for analysis and visualization of functional magnetic resonance neuroimages. Comput Biomed Res 1996;29:162–173. [PubMed: 8812068]

Cox RW, Hyde JS. Software tools for analysis and visualization of fMRI data. NMR Biomed 1997;10:171–178. [PubMed: 9430344]

DeZwart JA, Ledden PJ, van Gelderen P, Bodurka J, Chu R, Duyn JH. Signal-to-noise ratio and parallel imaging performance of a 16-channel receive-only brain coil array at 3.0 Tesla. Magn Reson Med 2004;51:22–6. [PubMed: 14705041]

Eblen F, Graybiel AM. Highly restricted origin of prefrontal cortical inputs to striosomes in the macaque monkey. J Neurosci 1995;15:5999–6013. [PubMed: 7666184]

Eriksson H, Gillberg PG, Aquilonius SM, Hedstrom KG, Heilbronn E. Receptor alterations in manganese intoxicated monkeys. Arch Toxicol 1992;66:359–364. [PubMed: 1319135]

Eriksson H, Magiste K, Plantin LO, Fonnum F, Hedstrom KG, Theodorsson-Norheim E, Kristensson K, Stalberg E, Heilbronn E. Effects of manganese oxide on monkeys as revealed by a combined neurochemical, histological and neurophysiological evaluation. Arch Toxicol 1987;61:46–52. [PubMed: 3439874]

Ferry AT, Ongur D, An X, Price JL. Prefrontal cortical projections to the striatum in macaque monkeys: evidence for an organization related to prefrontal networks. J Comp Neurol 2000;425:447–470. [PubMed: 10972944]

Forman SD, Cohen JD, Fitzgerald M, Eddy WF, Mintun MA, Noll DC. Improved assessment of significant activation in functional magnetic resonance imaging (fMRI): use of a cluster-size threshold. Magn Reson Med 1995;33:636–647. [PubMed: 7596267]

Haber SN, Kunishio K, Mizobuchi M, Lynd-Balta E. The orbital and medial prefrontal circuit through the primate basal ganglia. J Neurosci 1995;15:4851–4867. [PubMed: 7623116]

Haber SN, Kim KS, Mailly P, Calzavara R. Reward-related cortical inputs define a large striatal region in primates that interface with associative cortical connections, providing a substrate for incentive-based learning. J Neurosci 2006;26:8368–8376. [PubMed: 16899732]

Hays AV, Richmond BJ, Optican LMA. Unix-based multiple process system for real-time data acquisition and control. WESCON 1982;2:1–10.

Hoover JE, Strick PL. Multiple output channels in the basal ganglia. Science 1993;259:819–821. [PubMed: 7679223]

Kelly RM, Strick PL. Rabies as a transneuronal tracer of circuits in the central nervous system. J Neurosci Methods 2000;103:63–71. [PubMed: 11074096]

Kunishio K, Haber SN. Primate cingulostriatal projection: limbic striatal versus sensorimotor striatal input. J Comp Neurol 1994;350:337–356. [PubMed: 7533796]

Leergaard TB, Bjaalie JG, Devor A, Wald LL, Dale AM. In vivo tracing of major rat brain pathways using manganese-enhanced magnetic resonance imaging and three-dimensional digital atlasing. Neuroimage 2003;20:1591–1600. [PubMed: 14642470]

Murayama Y, Weber B, Saleem KS, Augath M, Logothetis NK. Tracing neural circuits in vivo with Mn-enhanced MRI. Magn Reson Imaging 2006;24:349–358. [PubMed: 16677940]

Olanow CW, Good PF, Shinotoh H, Hewitt KA, Vingerhoets F, Snow BJ, Beal MF, Calne DB, Perl DP. Manganese intoxication in the rhesus monkey: a clinical, imaging, pathologic, and biochemical study. Neurology 1996;46:492–498. [PubMed: 8614520]

Pal PK, Samii A, Calne DB. Manganese neurotoxicity: a review of clinical features, imaging and pathology. Neurotoxicology 1999;20:227–238. [PubMed: 10385886]

Pautler RG. In vivo, trans-synaptic tract-tracing utilizing manganese-enhanced magnetic resonance imaging (MEMRI). NMR Biomed 2004;17:595–601. [PubMed: 15761948]

Pautler RG, Silva AC, Koretsky AP. In vivo neuronal tract tracing using manganese-enhanced magnetic resonance imaging. Magn Reson Med 1998;40:740–748. [PubMed: 9797158]

Pautler RG, Mongeau R, Jacobs RE. In vivo trans-synaptic tract tracing from the murine striatum and amygdala utilizing manganese enhanced MRI (MEMRI). Magn Reson Med 2003;50:33–39. [PubMed: 12815676]

Saleem KS, Pauls JM, Augath M, Trinath T, Prause BA, Hashikawa T, Logothetis NK. Magnetic resonance imaging of neuronal connections in the macaque monkey. Neuron 2002;34:685–700. [PubMed: 12062017]

Selemon LD, Goldman-Rakic PS. Longitudinal topography and interdigitation of corticostriatal projections in the rhesus monkey. J Neurosci 1985;5:776–794. [PubMed: 2983048]

Silva AC, Lee JH, Aoki I, Koretsky AP. Manganese-enhanced magnetic resonance imaging (MEMRI): methodological and practical considerations. NMR Biomed 2004;17:532–543. [PubMed: 15617052]

Simmons JM, Richmond BJ. Dynamic changes in representations of preceding and upcoming reward in monkey orbitofrontal cortex. Cereb Cortex 2008;18:93–103. [PubMed: 17434918]

Sloot WN, Gramsbergen JB. Axonal transport of manganese and its relevance to selective neurotoxicity in the rat basal ganglia. Brain Res 1994;657:124–132. [PubMed: 7820609]

Sloot WN, van der Sluijs-Gelling AJ, Gramsbergen JB. Selective lesions by manganese and extensive damage by iron after injection into rat striatum or hippocampus. J Neurochem 1994;62:205–216. [PubMed: 7505311]

Strick, PL.; Card, JP. Transneuronal mapping of neural circuits with alpha herpesviruses. In: Bolam, JP., editor. Experimental Neuroanatomy: A Practical Approach. Oxford: Oxford University Press; 1992. p. 81-101.

Thorpe SJ, Rolls ET, Maddison S. The orbitofrontal cortex: Neuronal activity in the behaving monkey. Exp Brain Res 1983;49:93–115. [PubMed: 6861938]

Tremblay L, Schultz W. Reward-related neuronal activity during go-nogo task performance in primate orbitofrontal cortex. J Neurophysiol 2000;83:1864–1876. [PubMed: 10758098]

Van der Linden A, Verhoye M, Van Meir V, Tindemans I, Eens M, Absil P, Balthazart J. In vivo manganese-enhanced magnetic resonance imaging reveals connections and functional properties of the songbird vocal control system. Neuroscience 2002;112:467–474. [PubMed: 12044464]

Van der Zijden JP, Bouts MJ, Wu O, Roeling TA, Bleys RL, van der Toorn A, Dijkhuizen RM. Manganese-enhanced MRI of brain plasticity in relation to functional recovery after experimental stroke. J Cereb Blood Flow Metab. 2007

Van Meir V, Verhoye M, Absil P, Eens M, Balthazart J, Van der Linden A. Differential effects of testosterone on neuronal populations and their connections in a sensorimotor brain nucleus controlling song production in songbirds: a manganese enhanced-magnetic resonance imaging study. Neuroimage 2004;21:914–923. [PubMed: 15006658]

Watanabe T, Michaelis T, Frahm J. Mapping of retinal projections in the living rat using high-resolution 3D gradient-echo MRI with Mn2+-induced contrast. Magn Reson Med 2001;46:424–429. [PubMed: 11550231]

Watanabe T, Frahm J, Michaelis T. Functional mapping of neural pathways in rodent brain in vivo using manganese-enhanced three-dimensional magnetic resonance imaging. NMR Biomed 2004;17:554–568. [PubMed: 15617054]

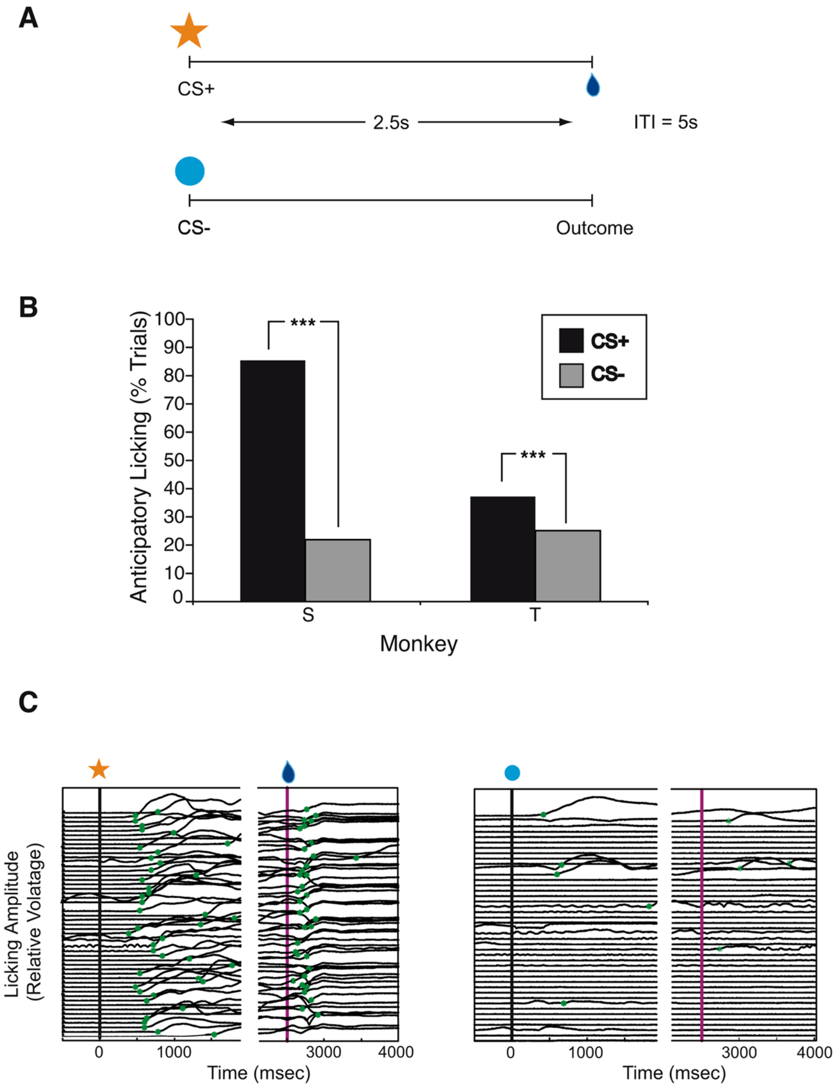

Figure 1.

Classical conditioning paradigm and behavioral results after isotonic $MnCl_2$ injections. **A.** Schematic of the classical conditioning paradigm. Each trial consisted of the presentation of a visual stimulus on a computer screen followed 2.5 seconds later by the trial outcome. In CS+ trials, the visual stimulus was an orange star, and the outcome was a liquid reward. In CS− trials, the visual stimulus was a blue circle, and the outcome was no reward. Trials were presented in random order. Inter-trial intervals (ITI) were 5 seconds in length. **B.** Percentages of CS+ (black bars) vs CS− (gray bars) trials with in anticipatory licking. Both monkeys S and T showed significantly more anticipatory licking in CS+ trials, as expected. **C.** Licking amplitude (changes in voltage measured by a strain gauge) as a function of time in a single behavioral session for monkey S. The left panel shows all of the CS+ trials in this session; the right panel shows all of the CS− trials. The timing of significant increases in amplitude is marked with green stars. Anticipatory licking began more than 1 second before trial outcome in the CS+ trials, but not in most of the CS− trials. Licking also increases after the delivery of the reward in CS+ trials.

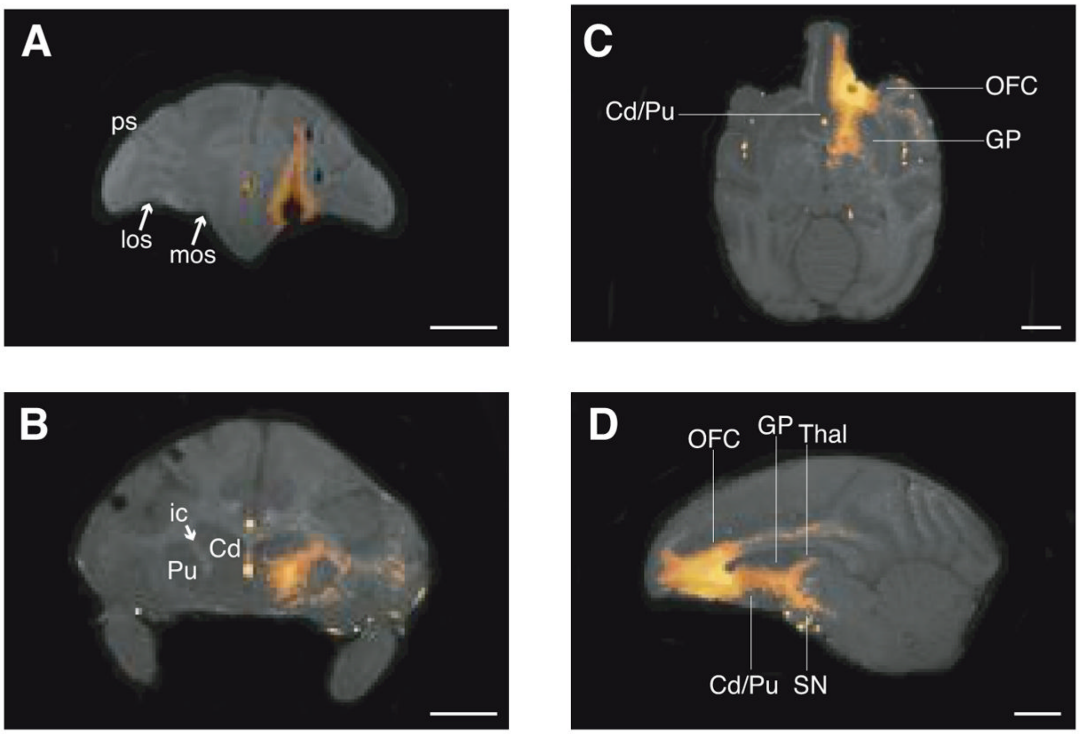

Figure 2.

Manganese transport images after injections of high concentration (800mM) $MnCl_2$ into orbitofrontal cortex (OFC) of monkey P. All images acquired at 4.7T with 0.5 mm^3 resolution (TR100 msec, TE 3.5 msec, flip angle 45°). Mn^{2+}-related signal enhancements due to shortened T_1 were easily seen by eye as bright white voxels. These voxels have been highlighted using the “Fire” color lookup table from ImageJ (Abramoff et al., 2004). **A.** The injection site within 3 hours of the $MnCl_2$ injection, in the coronal plane. The central portion of the injection site appears black due to the very short T2 that occurs in areas of very high concentration Mn^{2+}. The injection site covered most of OFC area 13 and extended into the white matter directly above OFC. los: lateral orbital sulcus; mos: medial orbital sulcus; ps: principal sulcus. **B.** Post-injection Day 4. Mn^{2+} transport from OFC to ventrolateral caudate (Cd) and ventromedial putamen (Pu) via the internal capsule (ic), in the coronal plane. **C.** Post-injection Day 4. Mn^{2+} transport from OFC to striatum via the internal capsule, in the horizontal plane. Thin lines indicate rostro-caudal levels of the OFC injection site, caudate-putamen (Cd/Pu), and globus pallidus (GP). **D.** Post-injection Day 4. Mn^{2+} transport throughout the orbitofrontal-striatal-thalamic loop, in the sagittal plane. Thin lines indicate rostro-caudal levels of the OFC injection site, caudate-putamen, globus pallidus, substantia nigra (SN) and thalamus (Thal). Length of all scale bars = 10 mm.

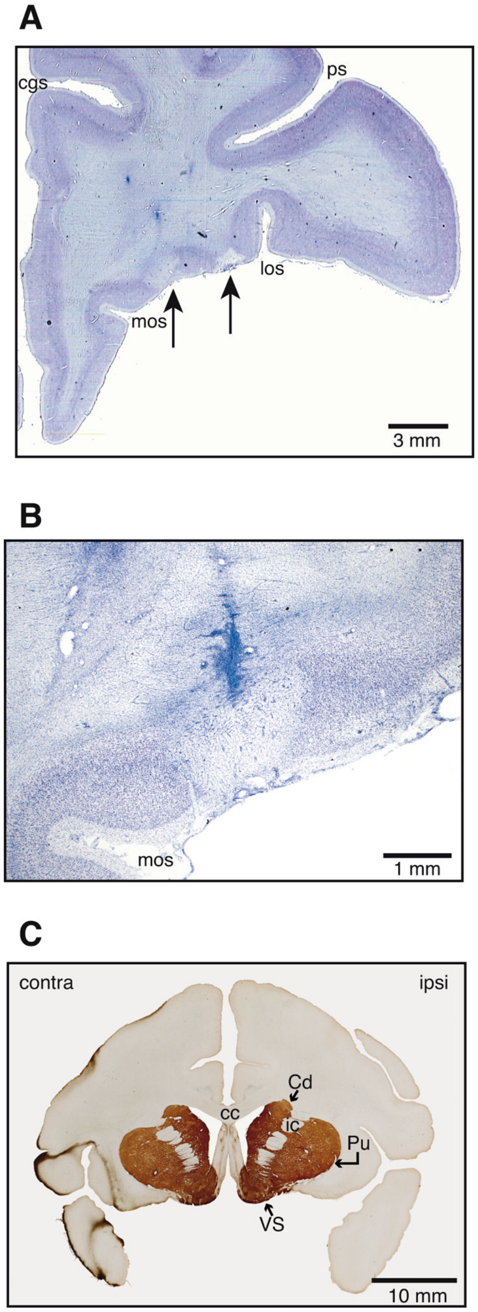

Figure 3.

Histological findings after injections of high concentration (800mM) $MnCl_2$ in OFC of monkey P. **A.** Thionin staining revealed two areas of complete cell loss in OFC areas corresponding to injection locations. cgs: cingulate sulcus; los: lateral orbital sulcus; mos: medial orbital sulcus; ps: principal sulcus. **B.** Higher power view of the more medial lesion shown in A. This lesion falls within the injection site shown in Figure 2A. The needle track itself is also visible. **C.** Immunocytochemistry revealed no differences in tyrosine hydroxylase levels in ipsilateral striatal targets of manganese transport versus the corresponding contralateral areas. Cd: caudate; Pu: putamen; VS: ventral striatum; cc: corpus callosum; ic: internal capsule.

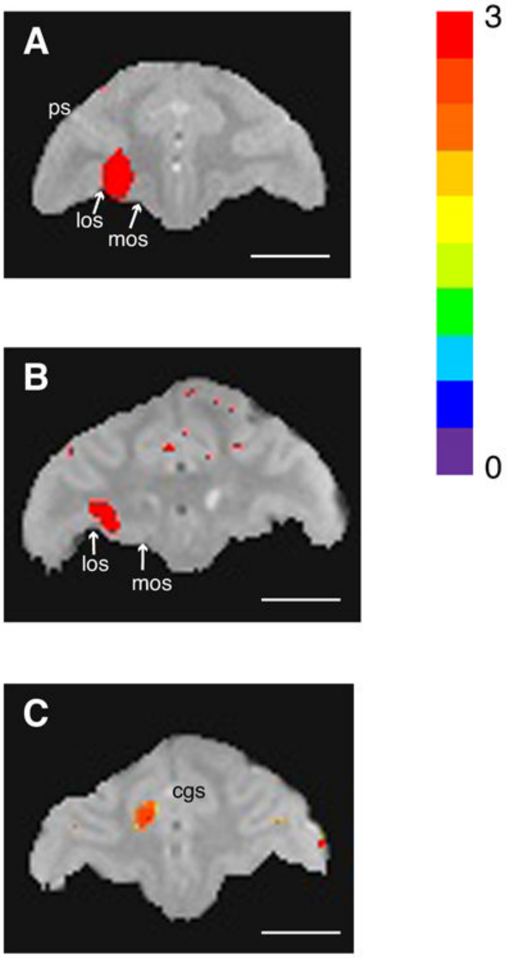

Figure 4.

Localization of isotonic (120 mM) $MnCl_2$ within 3 hours of injection. **A.** Orbitofrontal injection site in monkey T. **B.** Orbitofrontal injection site in monkey S. Orbitofrontal injections were localized to the lateral half of area 13 in both monkeys, with some extension into the overlying white matter. los: lateral orbital sulcus; mos: medial orbital sulcus; ps: principal sulcus. **C:** Anterior cingulate injection site in monkey S. The injection site was located ventral to the cingulate sulcus in area 24c. All images acquired at 4.7T with 0.5 mm^3 resolution, and sequence parameters: TR100 msec, TE 3.5 (monkey S) or 4.7 msec (monkey T), apparent flip angle 45°. Mn^{2+} signal intensity maps are superimposed on images from separate volumes acquired with sequence parameters designed to highlight gray-white matter contrast and anatomical landmarks (TR 100 msec, TE 6.5 msec, apparent flip angle 10°). Highlighted voxels are those with signal intensities at least two standard deviations from the pre-injection mean (color bar from 0 to 3 standard deviations). cgs: cingulate sulcus. Length of all scale bars = 10 mm.

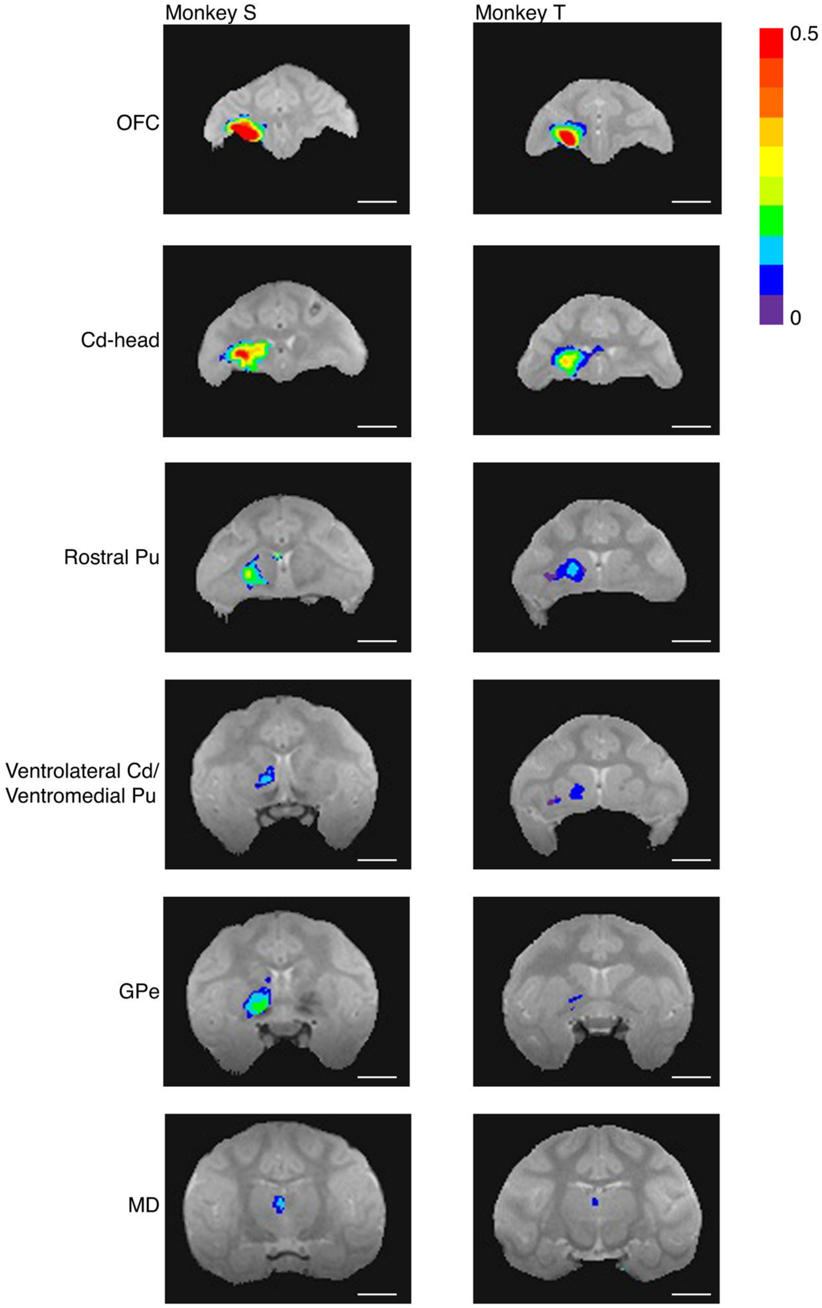

Figure 5.

Manganese transport on post-injection Day 2, after isotonic $MnCl_2$ injections into OFC of monkeys S and T. Signal intensity maps show enhancements ipsilaterally in OFC, in the head of the caudate nucleus (Cd-head) and rostral putamen (Pu), in ventrolateral caudate and ventromedial putamen, in globus pallidus externa (GPe), and in mediodorsal nucleus of the thalamus (MD; transport seen in the ventral anterior nucleus of the thalamus in monkey S not pictured). Image acquisition parameters as in Figure 4. Highlighted voxels are those with a statistically significantly greater mean signal intensity in post- versus pre-injection scans (t-test; $p <= .01$, all corrected for multiple comparisons except monkey T’s GPe and MD images). Colors denote the magnitude of the signal change. Length of all scale bars = 10 mm.

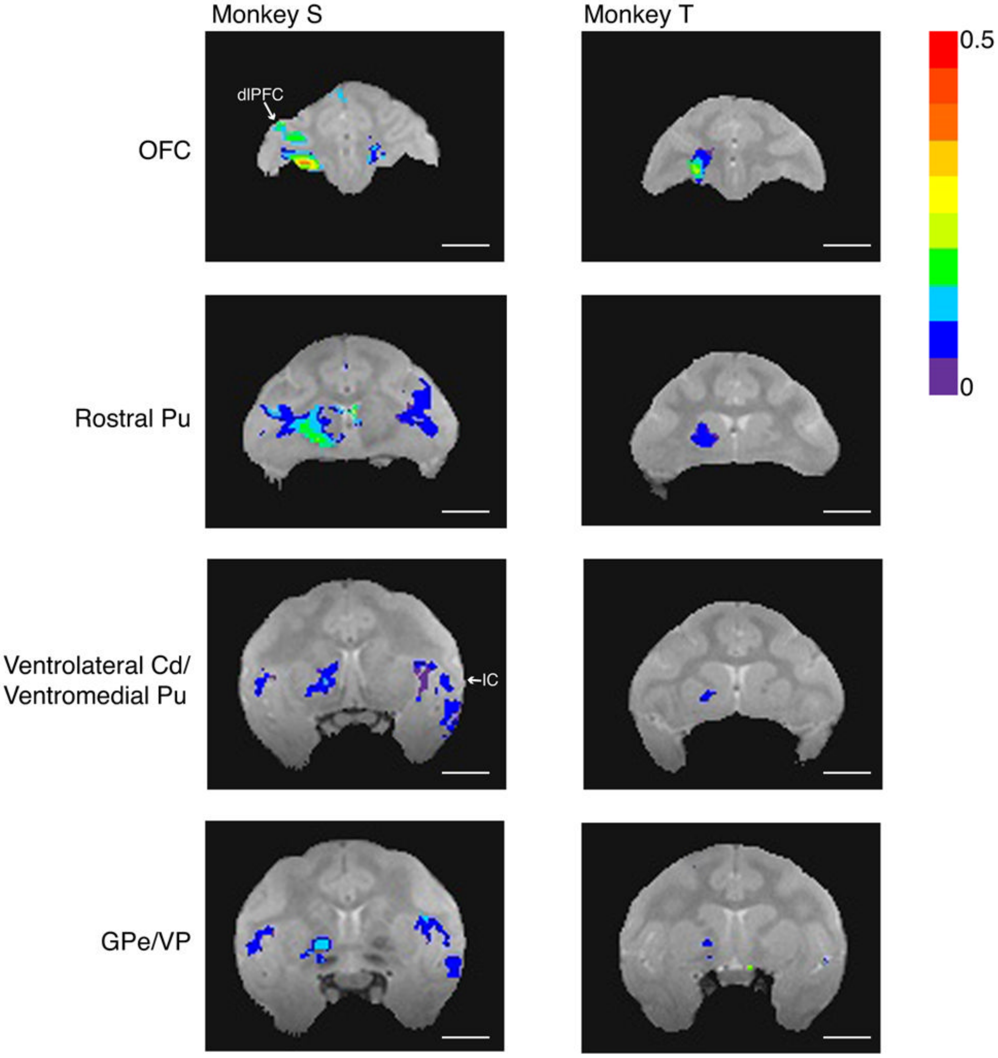

Figure 6.

Manganese transport on post-injection Day 4, after isotonic $MnCl_2$ injections into OFC of monkeys S and T Signal intensity maps show continued signal enhancements in OFC, transport to rostral putamen (Pu), ventrolateral caudate (Cd) and ventromedial putamen, and transport to globus pallidus externa (GPe) and ventral pallidum (VP). Signal intensities in subcortical targets are generally lower on Day 4 than on Day 2 (see Figure 5). In S, transport to ipsilateral dorsolateral prefrontal cortex (dlPFC) and bilateral insular cortex (IC) was detected for the first time on Day 4. Image acquisition parameters as in Figure 4. Statistical mapping conventions as in Figure 5 (all corrected for multiple comparisons except monkey T's GPe/VP image). Length of all scale bars = 10 mm.

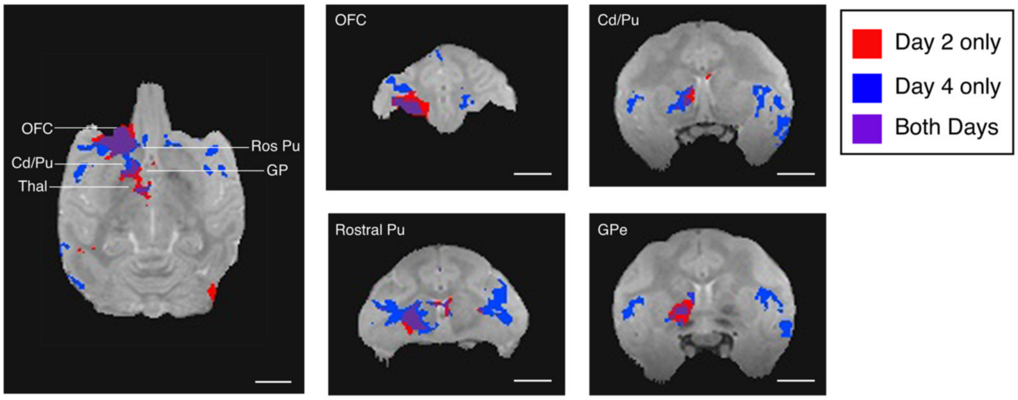

Figure 7.

Manganese transport over time. Topographic distribution of manganese signal on post-injection Day 2 (red) and Day 4 (blue) after injection of isotonic $MnCl_2$ into OFC of monkey S. Purple areas are those in which there was enhanced signal on both post-injection days. Note that subcortical targets of manganese transport overlapped extensively across time. Detection of manganese transport in cortical areas was greater on Day 4. These maps do not show the range of signal intensity differences visible in Figures 5 and 6. Thin lines on horizontal slice indicate rostro-caudal levels of OFC, rostral putamen (Ros Pu), ventrolateral caudate (Cd) and ventromedial putamen, globus pallidus (GP), and thalamus (Thal). Length of all scale bars = 10 mm.

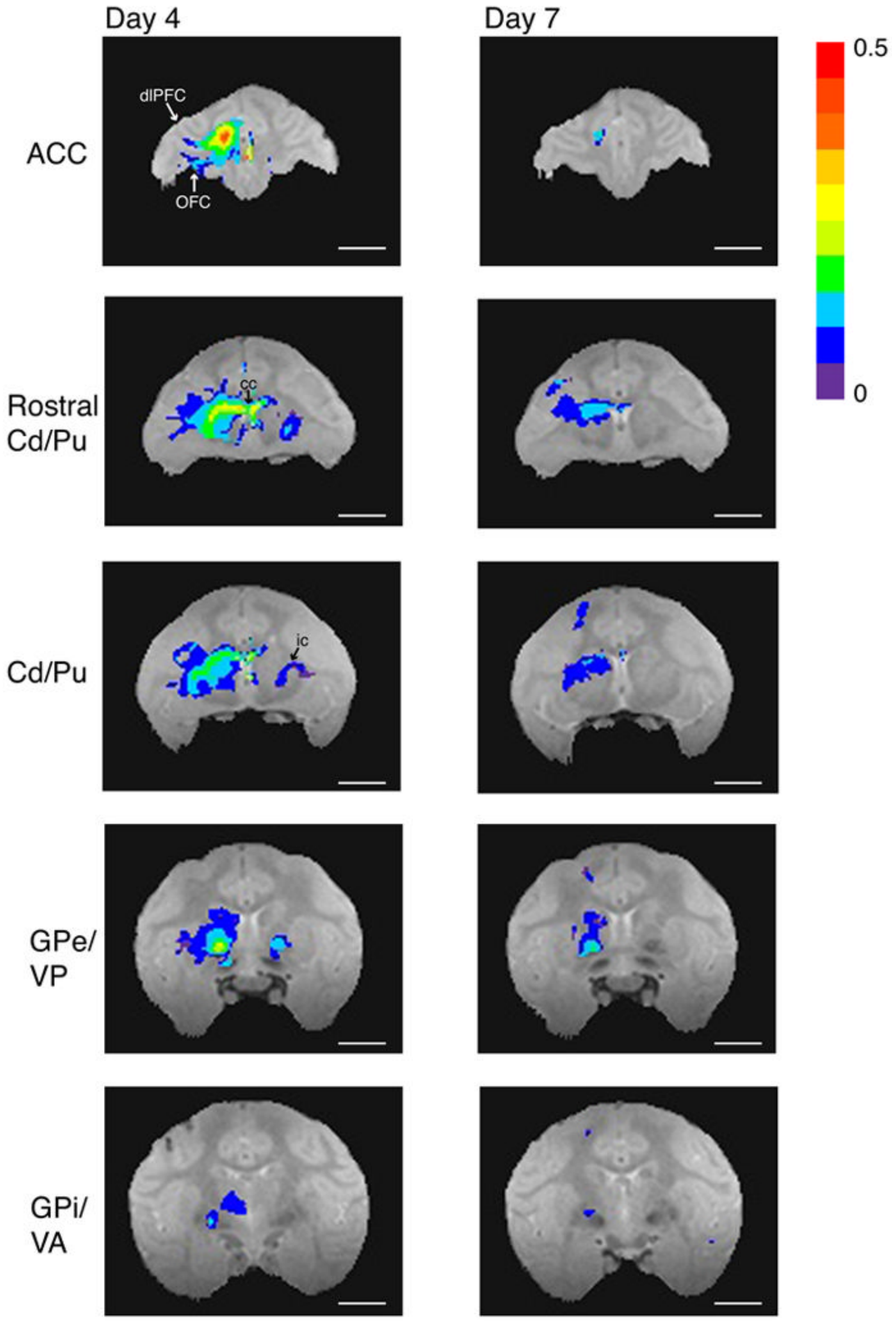

Figure 8.

Manganese transport after isotonic $MnCl_2$ injections into anterior cingulate cortex (ACC) of monkey S. On post-injection Day 4, manganese was detected ipsilaterally throughout area 24c, in dorsolateral prefrontal cortex (dlPFC area 46V), orbitofrontal cortex (OFC area 13), and regions on the medial wall (areas 24b and 32). Subcortical signal was found ipsilaterally in dorsal caudate (Cd) and putamen (Pu), globus pallidus externa and interna (GPe/GPi), ventral pallisum (VP), and ventral anterior nucleus of the thalamus (VA; transport seen in the medial dorsal nucleus of the thalamus not pictured). There was also manganese signal within the corpus callosum (cc), and manganese accumulation contralateral to the injection site in the internal capsule (ic), rostral putamen, and globus pallidus externa. On post-injection Day 7, manganese signal remained around the injection site, in dorsal caudate and dorsal putamen, in globus pallidus externa and interna. Image acquisition parameters as in Figure 4. Statistical mapping conventions as in Figure 5 (t-test; p <=.01, all corrected for multiple comparisons). Length of all scale bars = 10 mm.

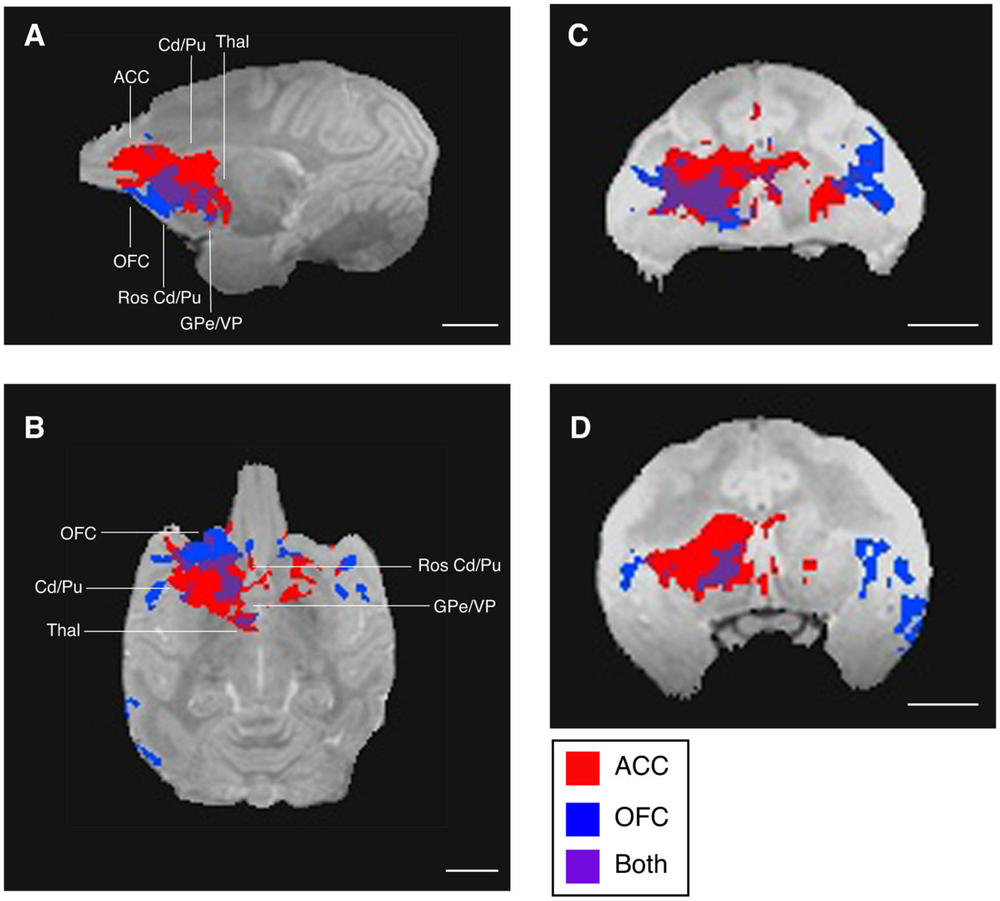

Figure 9.

Topographic distribution of manganese signal from anterior cingulate cortex (ACC; red) and orbitofrontal cortex (OFC; blue) after injections of isotonic $MnCl_2$ in monkey S. Purple areas are those to which both regions projected. Note that manganese transport after the ACC injection was more widespread than after the OFC injection and both regions projected to a set of common targets. **A.** Manganese signal after the OFC injection was located more ventrally than that after the ACC injection, as seen in the sagittal plane. **B.** Manganese signal after the OFC injection was more medially restricted than after the ACC injection, as seen in the horizontal plane. **C & D.** In striatum, manganese signal after the OFC injection was located more ventrally than after the ACC injection, as seen in the coronal plane. These maps do not show the range of signal intensity differences visible in Figures 6 and 8. Thin lines on sagittal and horizontal slices indicate rostro-caudal levels of OFC, ACC, caudate (Cd), putamen (Pu), globus pallidus externa (GPe), ventral pallidum (VP), and thalamus (Thal). Length of all scale bars = 10 mm.

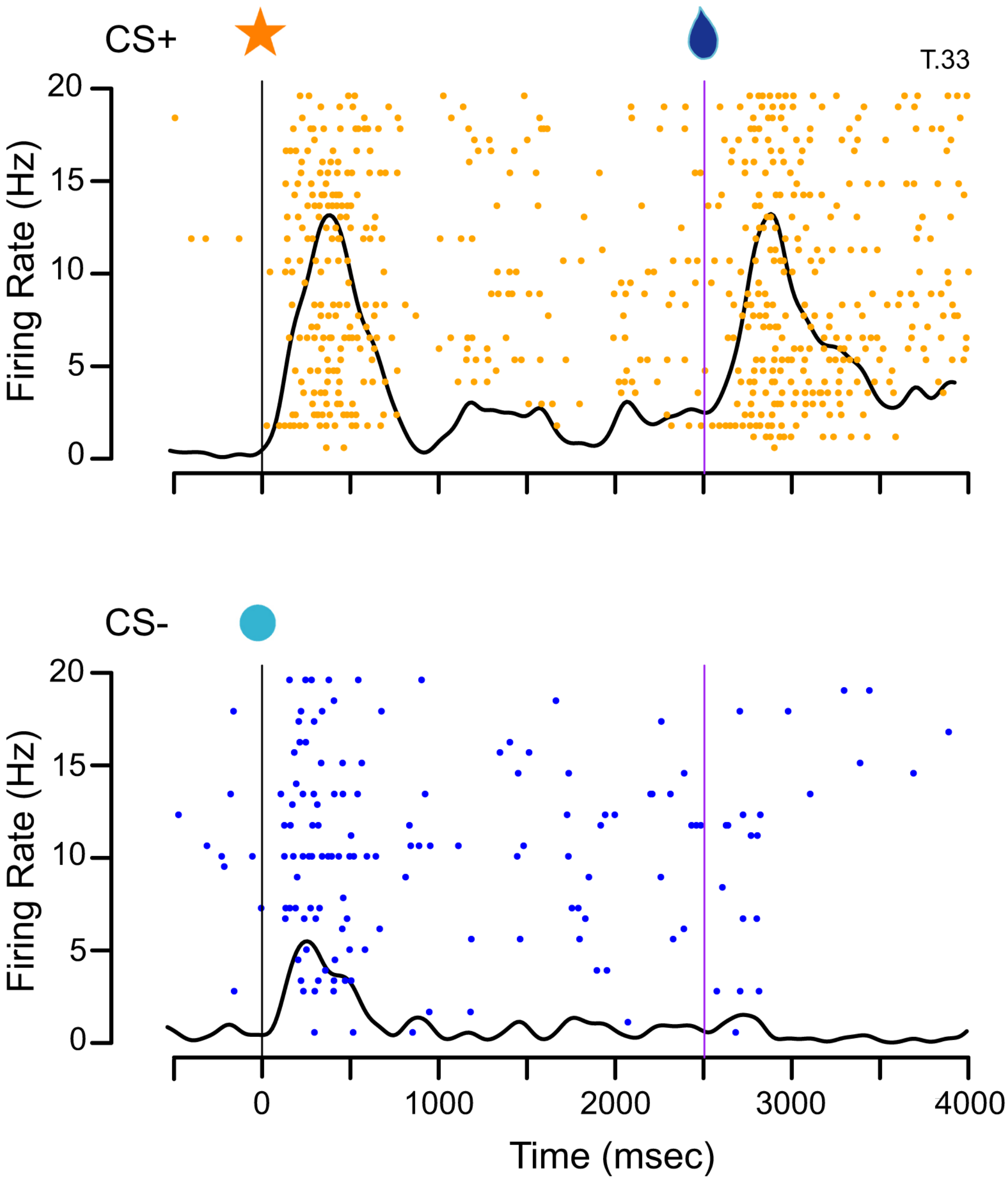

Figure 10.

Neuronal activity in orbitofrontal cortex after injections of isotonic $MnCl_2$. Single-unit activity was recorded while monkeys performed in the classical conditioning paradigm schematized in Figure 1. In this example from monkey T, a neuron within 1.4 mm of the injection site showed differential responses to both cues and outcomes in the CS+ (top) versus CS− (bottoms) trials. Rasters show firing rate (in Hz = spikes/second) as a function of time (in msec). Dots represent individual spikes, and each row corresponds to a different trial. Spike density function curves (Gaussian kernal, sd = 25 msec) are superimposed on each raster. Data are aligned at the time of the cue appearance (0 msec, leftmost vertical line); the trial outcome occurred at 2500 msec (rightmost vertical line).

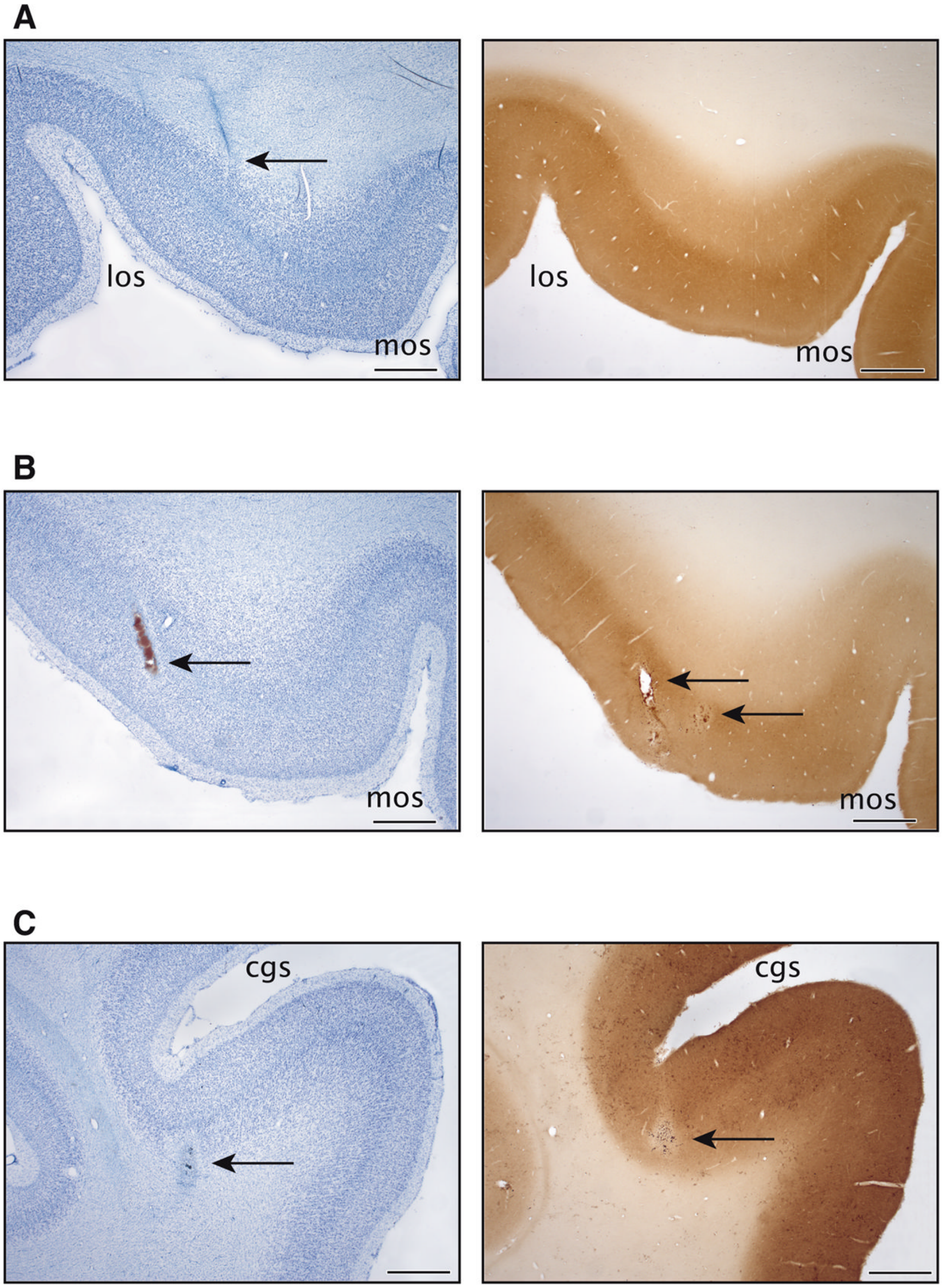

Figure 11.

Histological findings after injections of isotonic (120 mM) $MnCl_2$ in monkeys T and S. Panels on the left show thionin staining. Panels on the right show cytochome oxidase (CO) activity. **A.** Monkey T. Thionin staining revealed no areas of cell loss or damage after the orbitofrontal $MnCl_2$ injection. The needle track could be visualized, but the cortical tissue at the injection site could not be distinguished from the surrounding tissue. CO activity levels at the injection site also appeared unaffected. **B.** Monkey S. Thionin staining revealed no areas of cell loss after the orbitofrontal $MnCl_2$ injections. The needle itself did cause some tissue damage within OFC. CO activity levels appeared decreased in small regions near the injection sites. The tear from the needle itself can also be seen in this CO section. **C.** Monkey S. Thionin staining revealed a small area of cell loss after the anterior cingulate $MnCl_2$ injection. CO activity levels also appeared decreased in a small region near the injection site. Length of all scale bars = 1 mm.

Table 1

Monkey	Injection Location	$MnCl_2$ Concentration (mM)	$MnCl_2$ Volume (μL)	Number of Pre-injection Scans (# sessions)	Post-Injection Scanning Days[=]
P	OFC	800	0.5	0	0, 4
T	OFC	120	0.2	12 (7)	0, 2, 4
S	OFC	120	0.3	10 (7)	0[*], 2, 4
S	ACC	120	0.3	10 (7)	0, 4, 7

OFC: orbitofrontal cortex (area 13); ACC: anterior cingulate cortex (area 24c).

[=] Day 0: single scan; Days 2, 4, or 7: two scans at each time point.

[*] OFC injection in Monkey S made 11 weeks after ACC injection.